

Femtotesla Nearly-Quantum-Noise-Limited Pulsed Gradiometer at Earth-Scale Fields

V.G. Lucivero^{1,*}, W. Lee^{1D}, T.W. Kornack,² M.E. Limes,² E.L. Foley,² and M.V. Romalis¹

¹Department of Physics, Princeton University, Princeton, New Jersey 08544, USA

²Twinleaf LLC, Princeton, New Jersey 08544, USA



(Received 15 December 2021; revised 24 May 2022; accepted 8 July 2022; published 12 August 2022)

We describe a magnetic gradiometer that operates at finite fields and uses an intense pulsed laser to polarize a ^{87}Rb atomic ensemble and a compact vertical-cavity surface-emitting laser probe laser to detect paramagnetic Faraday rotation in a single multipass cell. We report differential magnetic sensitivity of $14 \text{ fT}/\text{Hz}^{1/2}$, corresponding to gradiometer sensitivity of $70 \text{ fT}/\text{cm}/\sqrt{\text{Hz}}$ with a 0.2 cm baseline, over a broad dynamic range, including Earth's field magnitude and a common-mode rejection ratio higher than 10^4 . We also observe a nearly quantum-noise-limited behavior of the gradiometer by comparing the experimental standard deviation of the estimated frequency difference against the Cramér-Rao lower bound in the presence of white photon shot-noise, atomic spin noise, and diffusion.

DOI: 10.1103/PhysRevApplied.18.L021001

a. Introduction.—Optically pumped magnetometers (OPMs) [1] have emerged as the most sensitive cryogen-free magnetic-field sensors in the last decade, providing a viable alternative to superconducting quantum interference devices (SQUIDs) [2–4], thanks to the achievement of subfemtotesla sensitivity [5–7] together with significant progress in sensor miniaturization [8,9]. More recently, optical magnetic gradiometers [10,11] have been developed for improving spatial information in near-zero field applications like magnetoencephalography (MEG) [12,13], as well as for effective ambient noise suppression in unshielded environments [14,15]. Operation in geomagnetic fields ($10 - 100 \mu\text{T}$) requires a high common-mode rejection ratio (CMRR) to achieve high sensitivity for applications in demanding environments [16], such as space magnetometry [17–19], magnetic navigation [20,21], archeological mapping [22,23], mineral exploration [24,25], searches for unexploded ordnance [26,27], and fundamental physics tests [28,29].

Multipass-cell-based magnetic gradiometers have reached sensitivities of $0.36 \text{ fT}/\text{cm}/\sqrt{\text{Hz}}$ at $7.3 \mu\text{T}$ [7] and $10.1 \text{ fT}/\text{cm}/\sqrt{\text{Hz}}$ at a medium-sized field of $26 \mu\text{T}$ [30], using either two 0.66 cm^3 cells or a single 10.8-cm^3 cell. Only a few intrinsic [31,32] (common noise rejected in one output) or synthetic [14,33] (subtraction of two OPMs outputs) gradiometers have reported operation around $50 \mu\text{T}$, i.e. Earth-field magnitude, with the best experimental sensitivity of $16 \text{ fT}/\text{cm}/\sqrt{\text{Hz}}$ with a 3-cm baseline, enabling detection of biomagnetism in the

ambient environment [14]. Due to additional technical noise sources such as rf broadband noise, pump, probe, or background field fluctuations, none of these gradiometers could attain experimental sensitivity at the quantum noise level. Operation near quantum limited sensitivity has been demonstrated at the near-zero field in biomagnetism [34], while quantum enhancement has been achieved by spin squeezing in rf magnetometry [35–37] and by squeezed light in a scalar optical magnetometer operating at $4.3 \mu\text{T}$ [38].

Here we describe a compact magnetic gradiometer using a 0.5-cm^3 single multipass cell, adjacent vertical-cavity surface-emitting laser (VCSEL) probe, and detection optics, that achieves quantum-noise-limited differential sensitivity of $14 \text{ fT}/\sqrt{\text{Hz}}$ over a broad dynamic range including $50 \mu\text{T}$ and CMRR higher than 10^4 , the best reported value for a magnetic gradiometer regardless of field dynamic range [11,14,39,40]. Due to a 0.2 cm baseline, the gradiometer sensitivity is $70 \text{ fT}/\text{cm}/\sqrt{\text{Hz}}$, comparable with state-of-the-art work at Earth-scale fields [14,31,32]. To match all these requirements, we operate our all-optical gradiometer in a synchronous light-pulse mode [41–43] under extreme conditions of intense pump power and pump pulse duration down to tens of nanoseconds. We also report experimental saturation of the standard deviation of the estimated frequency difference versus fitting time, in agreement with the Cramér-Rao lower bound due to white photon noise plus additional atomic noise. This distinguishing feature shows that the described Earth's field magnetic gradiometer is experimentally quantum-noise-limited, opening the possibility for quantum enhancement in geomagnetic fields by squeezed light [38,44,45] and spin squeezing [35,37,46,47] with femtotesla-level sensitivity.

*vito-giovanni.lucivero@icfo.eu Present address: ICFO-Institut de Ciències Fotoniques, The Barcelona Institute of Science and Technology, 08860 Castelldefels (Barcelona), Spain.

b. Sensor design and experimental setup.—The full experimental apparatus is shown in Fig. 1. The atomic sensor consists of a multipass vapor cell, fabricated through anodic bonding of glass windows and internal mirrors [48], fiberized optical heaters, a VCSEL probe laser, collimation and detection optics (not shown), and a quadrant photodiode. The cell is filled with pure ^{87}Rb and $p_{N_2} = 700$ Torr of N₂ buffer gas pressure. The effective interaction volume is 62 mm³. The compact sensor is housed within five layers of μ -metal magnetic shielding, with a set of cylindrical coils producing the main field B_z , as well as the first-order gradients $\partial B_z/\partial x$, $\partial B_z/\partial y$, and $\partial B_z/\partial z$. A semiconductor multimode pump laser, with a linewidth of 3 GHz, is tuned to the ^{87}Rb D_1 line. It is circularly polarized and aligned along the y axis to maximize initial atomic polarization. The pump laser works in a pulsed regime with an adjustable repetition rate, number of pulses, and width of pulses. The peak power is 2 W for a one microsecond pulse. When a finite B_z field is applied, to produce a resonant build-up of atomic spin orientation [41,42], we synchronize the pump repetition time with the Larmor period $T_{\text{pump}} = 1/\nu_L$, where $\nu_L = (\gamma/2\pi)B_z$ is the Larmor frequency and $\gamma = g_F\mu_B/\hbar$ is the gyromagnetic ratio. After a train of $N_{\text{pump}} = 10$ pulses of $\tau_{\text{pump}} = 1 \mu\text{s}$

width, the free induction decay (FID) of atomic polarization is probed by a VCSEL laser, which undergoes paramagnetic Faraday rotation and, after 15 reflections in a linear pattern without overlapping in the x - z plane, is detected by a dual-balanced polarimeter [39], consisting of compact polarization optics and four detectors, i.e., the active areas of a quadrant photodiode. As depicted in Fig. 1(b), the probe shape is elliptical with a width of 0.2 mm in the z direction and a height of 4 mm in the y direction, thus enabling a gradiometer detection of the gradient dB_z/dy with a 0.2-cm baseline, i.e., the spatial distance between the top and bottom half of the probe beam. This baseline is experimentally determined by applying a calibrated gradient and by measuring the distance between the two peaks in the fast Fourier transform of the signals from the two channels. The probe is blue-detuned by 100 GHz to optimize the trade-off between signal amplitude and spin relaxation due to residual probe absorption. The pump-probe cycle occurs repeatedly at a driving frequency of $f_d = 180$ Hz. After amplification with a transimpedance gain $G = 5 \times 10^4$ V/A, the two differential signals $V_{14} = V_1 - V_4$ and $V_{23} = V_2 - V_3$ are fed into a 24-bit digital oscilloscope (DAQ). In the absence of wrapping for small rotations ($\phi < \pi/4$) [49], mapping atomic FID evolution onto light probe polarization produces observed signals in the form of a sine wave with exponential decay:

$$V_{14}(t) = V_{23}(t) = V_0 \sin(2\pi\nu_L t + \delta) e^{-t/T_2}. \quad (1)$$

Here V_0 is the maximum amplitude and T_2 is the transverse relaxation rate. In Fig. 2 we report typical FID rotation signals from the two gradiometer channels and a sample fit to the function given in Eq. (1) for a shorter timescale. The temperature is optimized for sensitivity to 100 °C with a number density of 4.4×10^{12} atoms/cm³, measured via absorption spectroscopy [50].

c. Data analysis and results.—We acquired a FID train of signals for $T = 20$ sec with a $r_s = 5$ MHz sample rate. Then, we fit all signals in each gradiometer channel for a duration $T_m = 5$ ms to get a frequency difference array $\{\Delta\nu^{(i)}\}_{i=1,\dots,n}$. Each sample is temporally spaced by $\tau_d = 1/f_d \approx 5.5$ msec. In Fig. 3(top) we report the results in the frequency domain, by showing the gradiometer magnetic spectral noise density $\rho_{\Delta B}(v) = (2\pi/v)\sigma_{\Delta\nu}/\sqrt{\Delta f}$, i.e., the differential magnetic sensitivity in fT/ $\sqrt{\text{Hz}}$, at different finite fields, where $\sigma_{\Delta\nu}$ is the standard deviation of the estimated frequency difference and $\Delta f = 1/(2T_m)$ is the gradiometer bandwidth. Apart from the technical noise peak at 60 Hz, we experimentally measured a differential sensitivity of 14 fT/ $\sqrt{\text{Hz}}$ over a broad dynamic range [51]. In fact, the magnetic noise floor does not change when the main field B_z is increased by an order of magnitude from 5 μT up to 50 μT , i.e., Earth's field magnitude. To keep the sensitivity high for fast precession, where $\nu_L \gg 1/T_2$, and

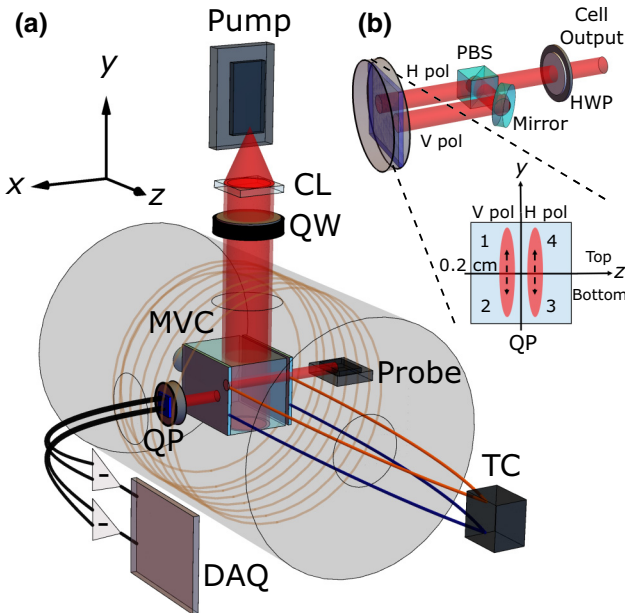


FIG. 1. (a) Schematic of the experiment. CL, cylindrical lens; QW, quarter-wave plate; HWP, half-wave plate; PBS, polarizing beam splitter; MVC, multipass vapor cell; TC, temperature controller; QP, quadrant photodiode; DAQ, data acquisition card. (b) Dual-balanced polarimeter. The elliptical probe impinges on the active areas (1-4) of the quadrant photodiode with either horizontal (H pol) or vertical polarization (V pol), after undergoing Faraday rotation in the multipass cell and detection by a balanced polarimeter.

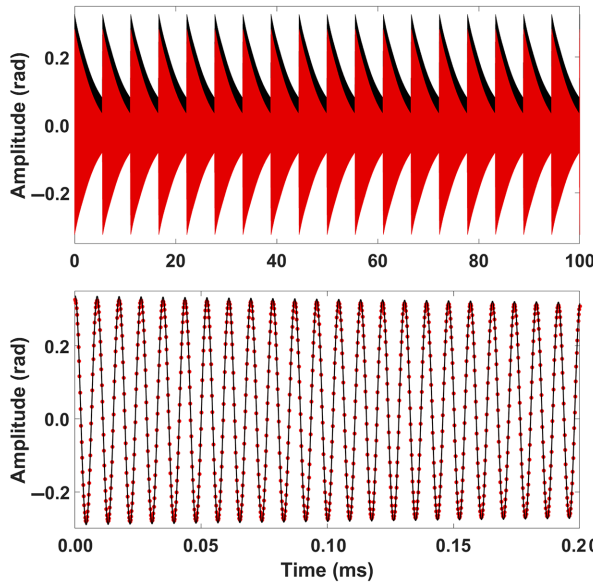


FIG. 2. (Top) Experimental signals. The rotation signals of the two channels V_{14} (back, black) and V_{23} (front, red) acquired from the digital oscilloscope at field $B_z = 16 \mu\text{T}$ and 400- μW total probe power. (Bottom) Short time signal and fit. Enlargement of the rotation signal (red points) and fit result (black continuous line) for the initial 0.2 ms.

to avoid atomic depolarization by the pump, we gradually decrease the width τ_{pump} of the pump pulses while increasing their total number, e.g., $N_{\text{pump}} = 150$ and $\tau_{\text{pump}} = 50 \text{ ns}$ at $B_z = 50 \mu\text{T}$, optimizing in this way the pump power per cycle for efficient polarization. The sensitivity can be alternatively obtained by directly computing the standard deviation of the frequency difference $\{\Delta\nu^{(i)}\}_{i=1,\dots,n}$ after averaging out the 60-Hz noise and calculating the short-term difference between successive points. The results of this equivalent analysis are shown in the inset of Fig. 3(top) and agree with the $14 \text{ fT}/\sqrt{\text{Hz}}$ spectral noise floor within uncertainty.

In Fig. 3(bottom) we report a sample signal of the atomic gradiometer, obtained by applying a 25 Hz modulation to the magnetic coil gradient dB_z/dy with an amplitude of 21.7 pT/cm. The figure shows the experimental noise spectral density with the applied gradient signal arising above the same noise floor of $14 \text{ fT}/\sqrt{\text{Hz}}$. Furthermore, we measure the CMRR of the gradiometer by applying a 6 Hz modulation to a dc magnetic field. The modulation amplitude is $1.4 \mu\text{T}$ for the field parallel to the pump alignment B_y and $1.8 \mu\text{T}$ for the transverse field B_z . The ratio of the signal peak amplitude in the magnetometer (single channel) over the amplitude in the differential gradiometer spectral density gives the measured CMRR. In the inset of Fig. 3(bottom) we show the measurement when the modulation is applied in the B_z main field. We measured the best CMRR of 1.2×10^4 and 2.9×10^4 for 6 Hz modulation

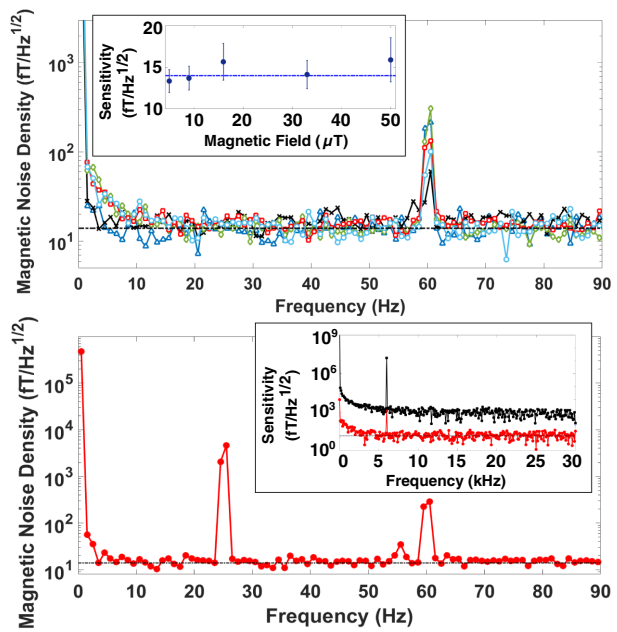


FIG. 3. (Top) Gradiometer sensitivity. Experimental magnetic noise spectral density at finite fields of $5 \mu\text{T}$ (blue triangles), $9 \mu\text{T}$ (black crosses), $16 \mu\text{T}$ (green diamonds), $33 \mu\text{T}$ (red squares), and $50 \mu\text{T}$ (cyan circles). (Inset) Magnetic noise density (blue points) is directly estimated (see text) versus the main field magnitude. Sensitivity reference of $14 \text{ fT}/\sqrt{\text{Hz}}$ (dot-dashed line) in both the main plot and inset. (Bottom) Gradiometer signal. Experimental noise spectral density for an applied $\partial B_z/\partial y$ gradient oscillating at 25 Hz. Inset: CMRR. Magnetometer (black) and gradiometer (red) noise density for an applied B_z oscillating at 6 Hz.

of the field in the two directions, respectively. This analysis shows good cancellation of broadband common field noise, as required for operation in an unshielded ambient environment, which in fact has been demonstrated by using a similar measurement scheme in a portable sensor with two multipass cells separated by a 3 cm baseline [14,52].

d. Fundamental theory and analysis.—The gradiometer fundamental noise contributions are due to photon shot noise and atomic spin noise [1]. In Fig. 4(a) we report the noise spectral density of a single gradiometer channel when the unpolarized ensemble is probed at $B_z = 16 \mu\text{T}$. A typical spin noise spectrum [53,54] with a peak noise density $\rho_{\text{at}} = 3.9 \times 10^{-7} V_{\text{rms}}/\sqrt{\text{Hz}}$ arises above a white photon shot-noise background $\rho_{\text{ph}} = 3.2 \times 10^{-7} V_{\text{rms}}/\sqrt{\text{Hz}}$, significantly above the electronic noise level. The photon shot-noise level agrees with its theoretical value [55] $\rho_{\text{ph}} = \sqrt{2G^2e\Re P}$, where G is the transimpedance gain, e is the electron charge, $\Re = 0.57 \text{ A/W}$ is the photodiode responsivity, and $P = 200 \mu\text{W}$ is the total optical power incident on the single channel. We compare the same noise spectrum in power density units, after subtracting white noise and shifting to zero frequency, to the analytical power spectrum $S(v) = \langle V_{\text{at}}^2 \rangle \int_{-\infty}^{\infty} C_d(\tau) e^{-(\tau/T_2 + 2\pi v\tau)} d\tau$

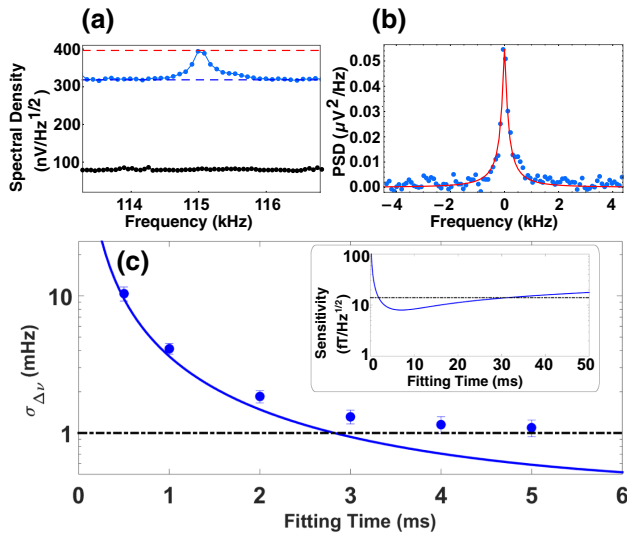


FIG. 4. (a) Noise spectral density. Experimental spin noise spectrum (blue points) at $B_z = 16 \mu\text{T}$. Atomic noise peak amplitude (dashed red line) and photon shot-noise background (blue line) with probe beam on. Experimental electronic noise (black points) with probe beam off. (b) Normalized power spectral density. Power spectral density (blue points) minus photon shot-noise background under same conditions of (a). Analytical power spectrum (red line) for 700 Torr of N_2 buffer gas and 0.2-mm beam radius. (c) Uncertainty of frequency difference. Experimental standard deviation of the gradiometer frequency difference (blue points) versus fitting time. Analytical CRLB (continuous blue curve) due to photon shot noise and best experimental result (dot-dashed line). Inset: the same curves of (c) in magnetic units for a longer fitting time.

in Fig. 4(b), where $\langle V^2 \rangle = (\rho_{\text{at}}^2 - \rho_{\text{ph}}^2)$ is the atomic noise power contribution and $C_d(\tau)$ is the contribution to the spin noise time-correlation function due to diffusion of atoms across the multipass probe beam [7,56]. By using the analytical solution of $C_d(\tau)$ obtained in [56], we found good agreement against data with no free parameters and a buffer gas pressure of $p_{\text{N}_2} = 700$ Torr, beam width $w = 0.2$ mm, and physical $l_{\text{cell}} = 10$ mm, where these quantities have been independently measured. This confirms that due to a diffusion time shorter than the intrinsic relaxation time T_2 the lineshape of the Lorentzian spin noise spectrum is broadened, giving a FWHM linewidth $\Delta\nu_c = 1/(\pi T_c)$ of about 290 Hz, where T_c is the noise correlation time including the effect of atomic diffusion across the probe beam. This linewidth is about 3.2 times larger than the linewidth due to the transverse relaxation time $T_2 = 3.5$ ms, obtained from the fit of the signals in Fig. 2.

To investigate the quantum-noise-limited behavior of the gradiometer sensitivity, we report the experimental standard deviation of the estimated frequency difference $\sigma_{\Delta\nu}$ versus fitting time T_m in Fig. 4(c). The theoretical Cramér-Rao lower bound (CRLB) for the estimation of the frequency of an exponentially damped sine wave in the presence of white gaussian noise has been obtained in

[57,58]. The minimum bound for the variance is

$$\sigma_{v,w}^2 \geq \frac{12\rho_w^2 C(T_m, T_2)}{(2\pi)^2 A^2 T_m^3}, \quad (2)$$

where $T_m = \Delta t N$ is the fitting time, Δt is the discrete sampling time, A is the signal amplitude, and $\rho_w = N_w / \sqrt{f_{\text{bw}}}$ is the spectral noise density, where N_w^2 is the gaussian noise variance and $f_{\text{bw}} = r_s/2$ is the detection bandwidth (or Nyquist frequency). The factor C , where $C = 1$ for a pure sine wave, takes into account the exponential decay and, in the limit $\Delta t \rightarrow 0$ (large N), is

$$C(T_m, T_2) = \frac{2T_m^3 e^{2\alpha} (e^{2\alpha} - 1)}{3T_2 (T_2^2 e^{4\alpha} + T_2^2 - 2e^{2\alpha} (T_2^2 + 2T_m^2))}, \quad (3)$$

where $\alpha = T_m/T_2$. For a gradiometer measurement, the final lower bound for the standard deviation of the estimated frequency difference is then given by

$$\sigma_{\Delta\nu,w}^{\text{CRLB}} \geq \sqrt{\sigma_{v1,w}^2 + \sigma_{v2,w}^2}, \quad (4)$$

where $\sigma_{v1,w}$ and $\sigma_{v2,w}$ are the lower bounds in the two channels in the presence of white noise only. In Fig. 4(c) we compare the experimental standard deviation $\sigma_{\Delta\nu}$, measured up to 5 ms, against the theoretical CRLB due to white photon shot noise. This is obtained with no free parameters by inserting in Eqs. (2), (3) and (4) experimental values of maximum signal amplitude $A = V_0$, spin relaxation $T_2 = 3.5$ ms, and rms noise density ρ_{ph} for both channels. The discrepancy depends on the fact that Eq. (2) does not include a second contribution due to the nonwhite atomic noise density ρ_{at} , which is comparable to the photon shot noise as the signal starts to decay above the spin-coherence time $T_2 = 3.5$ ms. However, the same saturation of the experimental standard deviation occurs over the entire investigated dynamic range, including $B_z = 50 \mu\text{T}$. This demonstrates that the pulsed magnetic gradiometer operates in a nearly quantum-noise-limited sensitivity regime. Finally, in the inset of Fig. 4(c) we report the CRLB due to photon shot noise in magnetic sensitivity units, which shows an optimal region of fitting time due to the magnetometer's bandwidth scaling. However, the experimental sensitivity saturates in shorter times due to the atomic spin noise, and the experimental fitting time is limited by the 180-Hz driving frequency of the pump-probe cycle. The extension of Eq. (2) to the presence of nonwhite noise is currently under theoretical investigation.

e. Conclusions and outlook.—We demonstrated a compact magnetic gradiometer operating in pulsed mode at finite fields with $14 \text{ fT}/\text{Hz}^{1/2}$ differential magnetic sensitivity over a broad dynamic range, 5 to $50 \mu\text{T}$, including Earth's field magnitude. The small 0.5-cm^3 cell volume represents a significant step forward in the

miniaturization of multipass-cell-based atomic sensors [7,30]. The high CMRR is suitable for applications in unshielded and challenging environments [14,16]. The sensitivity could be further improved with higher VCSEL laser power, while a technique for reducing heading errors due to the orientation of a total-field sensor has been recently developed [59]. A limitation to the accuracy is due to the short baseline of 0.2 cm, comparable with the quadrant photodiode active areas, can be overcome by employing separated beams probing the same cell [43,60] or two multipass cells [14]. However, since stretching the baseline in a two-beam or two-cell [31,32] geometry also reduces the CMRR due to the inherent addition of uncorrelated noise, further improvement could be made with the design of an all-optical and miniaturized version of a direct gradiometer using a single probe and a single multipass cell with intrinsic noise cancellation [30]. The operation mode of the described quantum-noise-limited gradiometer is compatible with quantum enhancement techniques using spin or polarization squeezing [38,61] in geomagnetic fields. The analysis at fields above 50 μT , due to nonlinear Zeeman effect and hyperfine splitting, will require further investigation.

Acknowledgements.—This work was supported by the Defense Advanced Research Projects Agency (DARPA). The views, opinions, and/or findings expressed are those of the authors and should not be interpreted as representing the official views or policies of the Department of Defense or the U.S. Government. During the manuscript writing, V. G. Lucivero has been supported by the H2020 Marie Skłodowska-Curie Action project PROBIST (Grant Agreement No. 754510).

-
- [1] D. Budker and M. Romalis, Optical magnetometry, *Nat. Phys.* **3**, 227 (2007).
 - [2] C. David, Magnetoencephalography: Detection of the brain's electrical activity with a superconducting magnetometer, *Science* **175**, 664 (1972).
 - [3] R. H. Koch, J. R. Rozen, J. Z. Sun, and W. J. Gallagher, Three squid gradiometer, *Appl. Phys. Lett.* **63**, 403 (1993).
 - [4] J.-H. Storm, D. Drung, M. Burghoff, and R. Körber, A modular, extendible and field-tolerant multichannel vector magnetometer based on current sensor squids, *Supercond. Sci. Technol.* **29**, 094001 (2016).
 - [5] I. K. Kominis, T. W. Kornack, J. C. Allred, and M. V. Romalis, A subfemtotesla multichannel atomic magnetometer, *Nature* **422**, 596 (2003).
 - [6] H. B. Dang, A. C. Maloof, and M. V. Romalis, Ultrahigh sensitivity magnetic field and magnetization measurements with an atomic magnetometer, *Appl. Phys. Lett.* **97**, 151110 (2010).
 - [7] D. Sheng, S. Li, N. Dural, and M. V. Romalis, Sub-femtotesla Scalar Atomic Magnetometry Using Multipass Cells, *Phys. Rev. Lett.* **110**, 160802 (2013).
 - [8] P. D. D. Schwindt, B. Lindseth, S. Knappe, V. Shah, J. Kitching, and L.-A. Liew, Chip-scale atomic magnetometer with improved sensitivity by use of the M_x technique, *Appl. Phys. Lett.* **90**, 081102 (2007).
 - [9] J. Kitching, Chip-scale atomic devices, *Appl. Phys. Rev.* **5**, 031302 (2018).
 - [10] K. Kim, S. Begus, H. Xia, S.-K. Lee, V. Jazbinsek, Z. Trontelj, and M. V. Romalis, Multi-channel atomic magnetometer for magnetoencephalography: A configuration study, *NeuroImage* **89**, 143 (2014).
 - [11] D. Sheng, A. R. Perry, S. P. Krzyzewski, S. Geller, J. Kitching, and S. Knappe, A microfabricated optically-pumped magnetic gradiometer, *Appl. Phys. Lett.* **110**, 031106 (2017).
 - [12] N. V. Nardelli, A. R. Perry, S. P. Krzyzewski, and S. A. Knappe, A conformal array of microfabricated optically-pumped first-order gradiometers for magnetoencephalography, *EPJ Quantum Technol.* **7**, 11 (2020).
 - [13] A. Borna, *et al.*, Non-invasive functional-brain-imaging with an OPM-based magnetoencephalography system, *PLoS ONE* **15**, 1 (2020).
 - [14] M. E. Limes, *et al.*, Portable Magnetometry for Detection of Biomagnetism in Ambient Environments, *Phys. Rev. Appl.* **14**, 011002 (2020).
 - [15] A. Jaufenthaler, *et al.*, Pulsed optically pumped magnetometers: Addressing dead time and bandwidth for the unshielded magnetorelaxometry of magnetic nanoparticles, *Sensors* **21**, 1212 (2021).
 - [16] K.-M. C. Fu, G. Z. Iwata, A. Wickenbrock, and D. Budker, Sensitive magnetometry in challenging environments, *AVS Quantum Sci.* **2**, 044702 (2020).
 - [17] M. K. Dougherty, *et al.*, Identification of a dynamic atmosphere at Enceladus with the Cassini magnetometer, *Science* **311**, 1406 (2006).
 - [18] I. Mateos, B. Patton, E. Zhivun, D. Budker, D. Wurm, and J. Ramos-Castro, Noise characterization of an atomic magnetometer at sub-millihertz frequencies, *Sens. Actuators A: Phys.* **224**, 147 (2015).
 - [19] H. Korth, *et al.*, Miniature atomic scalar magnetometer for space based on the rubidium isotope ^{87}rb , *J. Geophys. Res.: Space Phys.* **121**, 7870 (2016).
 - [20] J. A. Shockley and J. F. Raquet, Navigation of ground vehicles using magnetic field variations, *Navigation* **61**, 237 (2014).
 - [21] A. Canciani and J. Raquet, Airborne magnetic anomaly navigation, *IEEE Trans. Aerosp. Electron. Syst.* **53**, 67 (2017).
 - [22] A. David, M. Cole, T. Horsley, N. Linford, P. Linford, and L. Martin, A rival to Stonehenge? Geophysical survey at Stanton Drew, England, *Antiquity* **78**, 341 (2004).
 - [23] N. Linford, P. Linford, L. Martin, and A. Payne, Recent results from the English Heritage caesium magnetometer system in comparison with recent fluxgate gradiometers, *Archaeol. Prospect.* **14**, 151 (2007).
 - [24] M. N. Nabighian, V. J. S. Grauch, R. O. Hansen, T. R. LaFehr, Y. Li, J. W. Peirce, J. D. Phillips, and M. E. Ruder, 75th anniversary: The historical development of the magnetic method in exploration/historical development of magnetic method, *Geophysics* **70**, 33ND (2005).
 - [25] B. Gavazzi, L. Bertrand, M. Munsch, J. Mercier de Lépinay, M. Diraison, and Y. Géraud, On the use of aeromagnetism for geological interpretation: 1. Comparison of scalar and vector magnetometers for aeromagnetic surveys and an equivalent source interpolator for combining,

- gridding, and transforming fixed altitude and draping data sets, *J. Geophys. Res.: Solid Earth* **125**, e2019JB018870 (2020).
- [26] H. Nelson and J. McDonald, Multisensor towed array detection system for UXO detection, *IEEE Trans. Geosci. Remote Sens.* **39**, 1139 (2001).
- [27] V. Paoletti, A. Buggi, and R. Paštka, UXO detection by multiscale potential field methods, *Pure Appl. Geophys.* **176**, 4363 (2019).
- [28] I. Altarev, *et al.*, Test of Lorentz Invariance with Spin Precession of Ultracold Neutrons, *Phys. Rev. Lett.* **103**, 081602 (2009).
- [29] J. Lee, A. Almasi, and M. Romalis, Improved Limits on Spin-Mass Interactions, *Phys. Rev. Lett.* **120**, 161801 (2018).
- [30] V. G. Lucivero, W. Lee, N. Dural, and M. V. Romalis, Femtotesla Direct Magnetic Gradiometer Using a Single Multipass Cell, *Phys. Rev. Appl.* **15**, 014004 (2021).
- [31] R. Zhang, R. Mhaskar, K. Smith, and M. Prouty, Portable intrinsic gradiometer for ultra-sensitive detection of magnetic gradient in unshielded environment, *Appl. Phys. Lett.* **116**, 143501 (2020).
- [32] K. Campbell, Y.-J. Wang, I. Savukov, P. D. D. Schwindt, Y.-Y. Jau, and V. Shah, Gradient Field Detection Using Interference of Stimulated Microwave Optical Sidebands, *Phys. Rev. Lett.* **128**, 163602 (2022).
- [33] R. Zhang, *et al.*, Recording brain activities in unshielded Earth's field with optically pumped atomic magnetometers, *Sci. Adv.* **6**, eaba8792 (2020).
- [34] K. Jensen, *et al.*, Non-invasive detection of animal nerve impulses with an atomic magnetometer operating near quantum limited sensitivity, *Sci. Rep.* **6**, 29638 (2016).
- [35] W. Wasilewski, K. Jensen, H. Krauter, J. J. Renema, M. V. Balabas, and E. S. Polzik, Quantum Noise Limited and Entanglement-Assisted Magnetometry, *Phys. Rev. Lett.* **104**, 133601 (2010).
- [36] F. Martin Ciurana, G. Colangelo, L. Slodička, R. J. Sewell, and M. W. Mitchell, Entanglement-Enhanced Radio-Frequency Field Detection and Waveform Sensing, *Phys. Rev. Lett.* **119**, 043603 (2017).
- [37] H. Bao, *et al.*, Spin squeezing of 1011 atoms by prediction and retrodiction measurements, *Nature* **581**, 159 (2020).
- [38] C. Troullinou, R. Jiménez-Martínez, J. Kong, V. G. Lucivero, and M. W. Mitchell, Squeezed-Light Enhancement and Backaction Evasion in a High Sensitivity Optically Pumped Magnetometer, *Phys. Rev. Lett.* **127**, 193601 (2021).
- [39] G. Bevilacqua, V. Biancalana, P. Chessa, and Y. Dancheva, Multichannel optical atomic magnetometer operating in unshielded environment, *Appl. Phys. B* **122**, 103 (2016).
- [40] G. Oelsner, *et al.*, Integrated Optically Pumped Magnetometer for Measurements Within Earth's Magnetic Field, *Phys. Rev. Appl.* **17**, 024034 (2022).
- [41] W. E. Bell and A. L. Bloom, Optically Driven Spin Precession, *Phys. Rev. Lett.* **6**, 280 (1961).
- [42] V. Gerginov, S. Krzyzewski, and S. Knappe, Pulsed operation of a miniature scalar optically pumped magnetometer, *J. Opt. Soc. Am. B* **34**, 1429 (2017).
- [43] A. R. Perry, M. D. Bulatowicz, M. Larsen, T. G. Walker, and R. Wyllie, All-optical intrinsic atomic gradiometer with sub-20 fT/cm/ $\sqrt{\text{Hz}}$ sensitivity in a 22 μT earth-scale magnetic field, *Opt. Express* **28**, 36696 (2020).
- [44] F. Wolfgramm, A. Cerè, F. A. Beduini, A. Predojević, M. Koschorreck, and M. W. Mitchell, Squeezed-Light Optical Magnetometry, *Phys. Rev. Lett.* **105**, 053601 (2010).
- [45] V. G. Lucivero, R. Jiménez-Martínez, J. Kong, and M. W. Mitchell, Squeezed-light spin noise spectroscopy, *Phys. Rev. A* **93**, 053802 (2016).
- [46] J. Appel, *et al.*, Mesoscopic atomic entanglement for precision measurements beyond the standard quantum limit, *Proc. Nat. Acad. Sci.* **106**, 10960 (2009).
- [47] J. Kong, R. Jiménez-Martínez, C. Troullinou, V. G. Lucivero, G. Tóth, and M. W. Mitchell, Measurement-induced, spatially-extended entanglement in a hot, strongly-interacting atomic system, *Nat. Commun.* **11**, 2415 (2020).
- [48] N. Dural and M. V. Romalis, Anodically bonded cells with optical elements, US Patent 10345548 (2017).
- [49] S. Li, P. Vachaspati, D. Sheng, N. Dural, and M. V. Romalis, Optical rotation in excess of 100 rad generated by Rb vapor in a multipass cell, *Phys. Rev. A* **84**, 061403 (2011).
- [50] M. V. Romalis, E. Miron, and G. D. Cates, Pressure broadening of Rb D_1 and D_2 lines by ^3He , ^4He , N_2 , and Xe: Line cores and near wings, *Phys. Rev. A* **56**, 4569 (1997).
- [51] We do not divide the differential noise floor by additional $\sqrt{2}$, because such sensitivity level of 14 fT/ $\sqrt{\text{Hz}}$ is obtained directly from a differential frequency measurement and not inferred by a gradiometer sensitivity.
- [52] V. G. Lucivero, W. Lee, M. E. Limes, E. L. Foley, T. W. Kornack, and M. V. Romalis, in *Quantum Information and Measurement (QIM) V: Quantum Technologies* (Optica Publishing Group, 2019), p. T3C.3.
- [53] B. Aleksandrov and V. S. Zapasskii, Magnetic resonance in the faraday-rotation noi spectrum, *Sov. Phys. JETP* **54**, 64 (1981).
- [54] V. G. Lucivero, A. Dimic, J. Kong, R. Jiménez-Martínez, and M. W. Mitchell, Sensitivity, quantum limits, and quantum enhancement of noise spectroscopies, *Phys. Rev. A* **95**, 041803 (2017).
- [55] V. G. Lucivero, P. Anielski, W. Gawlik, and M. W. Mitchell, Shot-noise-limited magnetometer with sub-picotesla sensitivity at room temperature, *Rev. Sci. Instrum.* **85**, 113108 (2014).
- [56] V. G. Lucivero, N. D. McDonough, N. Dural, and M. V. Romalis, Correlation function of spin noise due to atomic diffusion, *Phys. Rev. A* **96**, 062702 (2017).
- [57] Y.-X. Yao and S. M. Pandit, Cramer-Rao lower bounds for a damped sinusoidal process, *IEEE Trans. Signal Process.* **43**, 878 (1995).
- [58] C. Gemmel, *et al.*, Ultra-sensitive magnetometry based on free precession of nuclear spins, *Eur. Phys. J. D* **57**, 303 (2010).
- [59] W. Lee, V. G. Lucivero, M. V. Romalis, M. E. Limes, E. L. Foley, and T. W. Kornack, Heading errors in all-optical alkali-metal-vapor magnetometers in geomagnetic fields, *Phys. Rev. A* **103**, 063103 (2021).
- [60] A. P. Colombo, T. R. Carter, A. Borna, Y.-Y. Jau, C. N. Johnson, A. L. Dagel, and P. D. D. Schwindt, Four-channel optically pumped atomic magnetometer for magnetoencephalography, *Opt. Express* **24**, 15403 (2016).
- [61] V. Shah, G. Vasilakis, and M. V. Romalis, High Bandwidth Atomic Magnetometry with Continuous Quantum Non-demolition Measurements, *Phys. Rev. Lett.* **104**, 013601 (2010).